Accurate numerical verification of the instanton method for macroscopic quantum tunneling: Dynamics of phase slips

Ippei Danshita[1,2,*] and Anatoli Polkovnikov[1]
[1]*Department of Physics, Boston University, Boston, Massachusetts 02215, USA*
[2]*Department of Physics, Faculty of Science, Tokyo University of Science, Shinjuku-ku, Tokyo 162-8601, Japan*
(Received 21 October 2009; revised manuscript received 10 August 2010; published 3 September 2010)

We study the quantum dynamics of supercurrents of one-dimensional Bose gases in a ring optical lattice to verify instanton methods applied to coherent macroscopic quantum tunneling (MQT). We directly simulate the real-time quantum dynamics of supercurrents, where a coherent oscillation between two macroscopically distinct current states occurs due to MQT. The tunneling rate extracted from the coherent oscillation is compared with that given by the instanton method. We find that the instanton method is quantitatively accurate when the effective Planck's constant is sufficiently small. We also find phase slips associated with the oscillations.

DOI: 10.1103/PhysRevB.82.094304 PACS number(s): 03.65.Xp, 03.75.Kk, 03.75.Lm, 67.85.−d

I. INTRODUCTION

Tunneling is one of the most fundamental concepts derived from quantum theory and is essential for understanding enormous variety of phenomena in different fields of physics, such as high energy, condensed matter, and atomic physics. The list of such phenomena includes the α decay of nuclei,[1] tunneling between vacuum states in quantum cosmology[2,3] and chromodynamics,[4–7] macroscopic quantum tunneling (MQT) in quantum gases[8,9] and condensed matter,[10,11] and also includes potential applications in quantum information.[12]

Instanton methods are general schemes describing quantum tunneling within a semiclassical approximation.[6,7,13] They are applicable to the broad range of problems listed above. These methods are based on the solution of the classical equations of motion in imaginary-time coordinate allowing one to obtain an analytical expression for the tunneling rate. The instanton methods are closely related to the Langer's formalism of decay of metastable states due to thermal fluctuations.[14] Given the versatility and utility of the instanton methods, it is important to examine how accurately they predict the actual tunneling rate. We note that this question is not entirely trivial. For example, for applicability of the Langer's formalism it is important that the thermal bath (which can be a part of the macroscopic system) is big enough to provide sufficient energy necessary to overcome the barrier separating metastable and stable phases.

For single particle problems, especially in one dimension, the instanton methods can be easily verified because the corresponding Schrödinger equation can be solved numerically with arbitrary precision. On the other hand, such numerical verification of the instanton methods is usually very difficult for complex systems consisting of many degrees of freedom, such as MQT and tunneling decay of the false vacuum. Alternatively, in the context of the current-biased Josephson junction, where the phase difference between the two superconductors is regarded as a macroscopic quantum variable, experiments have been extensively compared with the theory of MQT.[15,16] It has been shown that the experiments and the theory are in agreement to the extent that the instanton method provides an estimate on the order of the magnitude of the tunneling rate. However, this comparison is inevitably limited by the experimental uncertainty, which arises from the fact that the theory uses phenomenological parameters extracted from separate experiments.

Recent advances in experiments with cold atomic gases in an optical lattice have opened new possibilities for studying MQT phenomena. Specifically, strong inhibition of transport observed in one-dimensional (1D) Bose gases in a combined harmonic and optical lattice potential[17,18] has been interpreted as a manifestation of the decay of supercurrents due to MQT.[9,19] Moreover, further study of the supercurrent dynamics via MQT has been accelerated by the observation of persistent currents in a toroidal trap[20] and the realization of Bose-Einstein condensates in a ring optical lattice.[21] Since quantitative comparisons between experiments and microscopic theories are attainable in cold atom systems thanks to their unprecedented controllability, rigorous verification of the instanton method is imperative for accurately predicting the tunneling rate there.

In this work we study MQT of supercurrents of bosons in a 1D ring lattice to examine the validity of the instanton method applied to coherent MQT. We demonstrate that the time-evolving block decimation (TEBD) method,[22,23] which has been recently developed in the field of quantum information, allows for first principles simulations of the MQT dynamics of the corresponding Bose-Hubbard model even when the total number of particles is enormously large ($N \sim 10\,000$). Using this method, we show that the supercurrent exhibits coherent oscillations between two degenerate macroscopic states with different winding numbers. These oscillations are accompanied by phase slips which result in sudden change in the winding number characterizing the supercurrent. The tunneling rate is accurately extracted from the frequency of oscillations while it is also calculated by the instanton method in the quantum rotor limit corresponding to large filling factors.[9,24] We are thus able to compare the numerical TEBD results with the prediction of the instanton method with no ambiguity. Our main finding is that the instanton method gives a quantitatively correct value of the tunneling rate when the effective Planck's constant is suffi-

ciently small. We also find that the coherent oscillations of current persist even between the degenerate states with winding numbers different by two. Such process corresponds to the dynamics associated with coherent oscillations of double phase slips.

The remainder of the paper is organized as follows. In Sec. II, we introduce our model, the 1D ring Bose-Hubbard model with a phase twist. In Sec. III, using TEBD we simulate the quantum dynamics of supercurrents, which exhibits coherent oscillations via MQT. In Sec. IV, the quantum rotor model is derived from the Bose-Hubbard model in the limit of large filling factors. Applying the instanton method to the quantum rotor model, we calculate the tunneling rate in Sec. V. In Sec. VI. we finally present the comparison between the instanton and exact results. In Sec. VII, we summarize our results.

II. MODEL

We consider a system of N bosons at zero temperature confined in a homogeneous 1D ring lattice of L sites. Recently, such a system has been experimentally realized in the context of quantum gases.[21] We assume a sufficiently deep lattice so that the tight-binding approximation is valid. Then, the system is well described by the Bose-Hubbard model,[25]

$$\hat{H} = -J\sum_{j=1}^{L}(e^{-i\theta}\hat{b}_j^\dagger\hat{b}_{j+1} + \text{h.c.}) + \frac{U}{2}\sum_{j=1}^{L}\hat{n}_j(\hat{n}_j - 1), \qquad (1)$$

where $\hat{b}_{L+1} \equiv \hat{b}_1$, reflecting the periodic nature of the ring lattice. The field operator $\hat{b}_j^\dagger$ ($\hat{b}_j$) creates (annihilates) a boson on the jth site and $\hat{n}_j$ is the number operator. J is the hopping energy and U the onsite interaction. The phase twist θ can be controlled by rotating the lattice[26,27] (or equivalently by writing the Hamiltonian in the rotating frame) and θL corresponds to the flux through the ring. In the case of commensurate fillings, where the filling factor $\nu \equiv N/L$ is integer, the Bose-Hubbard model exhibits a quantum phase transition from a superfluid to a Mott insulator as U/J is increased. Since our interest is in the dynamics of supercurrents, we focus only on the superfluid regime throughout this paper.

III. SUPERCURRENT DYNAMICS

For pursuing our main goal of examining the validity of the instanton method, it is imperative to reveal basic properties of the quantum dynamics associated with Eq. (1). In this section, we confirm that a supercurrent flowing through the ring lattice actually exhibits MQT during the real-time evolution. In Sec. VI, we will compare the frequency of oscillations extracted from the MQT dynamics with that obtained by the instanton method.

To treat the quantum dynamics, we use the quasiexact numerical method of TEBD,[22] which is conceptually equivalent to the well-known time-dependent density matrix renormalization group.[28,29] This method allows us to compute accurately the evolution of many-body wave functions of 1D quantum lattice systems. Recently, TEBD has been successfully adopted by one of us to a system with periodic boundary conditions.[19] In order to study how a supercurrent behaves as a function of time, one needs to prepare a current-carrying state as an initial state of the real time evolution. For this purpose, setting $\theta = \theta_0 \equiv 2\pi n/L$, we first prepare the system in the ground state of Eq. (1), which is a current-carrying state with the winding number n. At $t=0$ the phase twist is suddenly shifted to $\theta_1 \equiv \pi(2n-l)/L$, $l \geq 1$, so that another state with the winding number $n-l$ is exactly degenerate with the initial state. We then simulate the dynamics in this system propagating the initial state in real time. First we analyze the situation where the filling factor and the initial winding number are equal to unity: $\nu=1$, $n=1$ and investigate how the time evolution of supercurrents depends on the parameters of the model U/J and θ_1.

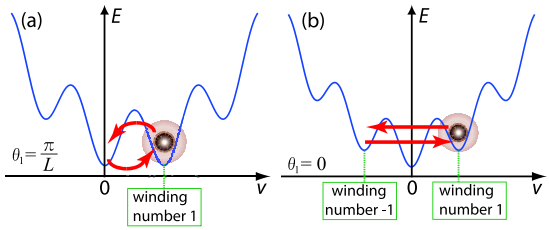

FIG. 1. (Color online) Sketch of the quantum dynamics of supercurrents in the effective potential obtained from the Bose-Hubbard Hamiltonian Eq. (1) for (a) $\theta_1 = \pi/L$ and (b) $\theta_1 = 0$. The blue solid lines sketch the energy landscape versus the current velocity v. The black circles represent the quantum state. Note that the plot represents a sketch of an actual process occurring in the multidimensional phase space.

Let us start with the simplest case, $\theta_1 = \pi/L$, where two macroscopically distinct states with winding numbers 1 and 0 are the degenerate lowest energy states. This situation is analogous to a superconducting flux qubit realized in a superconducting quantum interference device, where two flux states with different winding numbers are degenerate producing coherent Rabi oscillations.[12] Likewise in our case we expect coherent oscillations between the two degenerate states via MQT as sketched in Fig. 1(a) (see Appendix A for the origin of the tunneling coupling between the two states).

To demonstrate this, we first calculate the time evolution of the current velocity v given by

$$v = \frac{Jd}{i\hbar N}\sum_j \langle \hat{b}_j^\dagger \hat{b}_{j+1} - \text{h.c.}\rangle, \qquad (2)$$

where d is the lattice spacing. When $U/J \ll 1$, the velocity is almost constant, i.e., the supercurrent is persistent. In contrast, when U/J is sufficiently large, e.g., $U/J=2.5$, quantum fluctuations are strong enough to kick the state out from the one of the minima, and the superfluid coherently oscillates between the states with velocities $v(t=0)$ and 0 as shown in Fig. 2(a). The frequency of these oscillation increases monotonically with U/J.

To confirm that these oscillations are due to quantum tunneling between two macroscopically distinct states, we next calculate the overlap $|\langle \Phi_n | \Psi(t)\rangle|^2$ of the wave function with the ground state $|\Phi_n\rangle$ of the Hamiltonian (1) with $\theta = 2\pi n/L$, and the momentum occupation $n(p,t) = \langle \hat{\beta}_p^\dagger \hat{\beta}_p \rangle$,

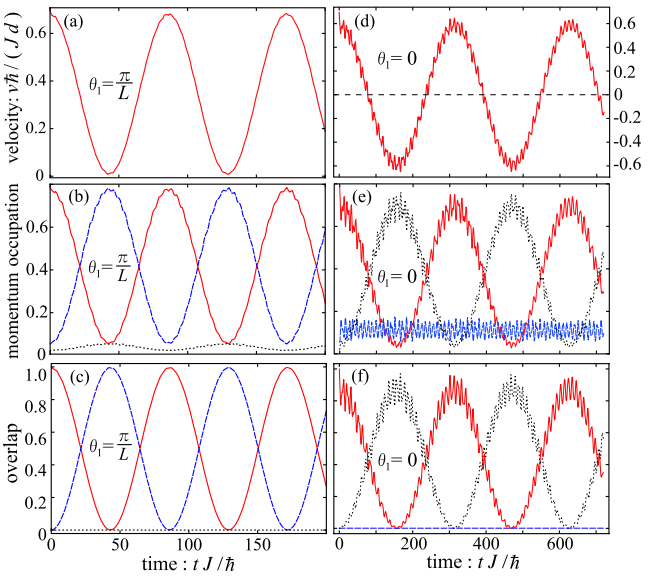

FIG. 2. (Color online) [(a) and (d)] Time evolution of the current velocity $v(t)$, [(b) and (e)] the momentum occupation $n(p,t)$, and [(c) and (f)] the overlap $|\langle\Phi_p|\Psi(t)\rangle|^2$. For $n(p,t)$ and $|\langle\Phi_p|\Psi(t)\rangle|^2$, the red solid, blue dashed, and black dotted lines correspond to $p=1$, 0, and -1. We set $L=N=16$ and $U/J=2.5$. In (a), (b), and (c), $\theta_1=\pi/L$ while in (d), (e), and (f) $\theta_1=0$.

where $\hat{\beta}_p=L^{-1/2}\Sigma_j\hat{b}_j e^{-i2\pi pj/L}$. In Fig. 2(c), we show the overlaps with $|\Phi_1\rangle$, $|\Phi_0\rangle$, and $|\Phi_{-1}\rangle$. The overlaps $|\langle\Phi_1|\Psi(t)\rangle|^2$ and $|\langle\Phi_0|\Psi(t)\rangle|^2$ are well approximated by the time dependence $\cos^2(\frac{\Delta}{2\hbar}t)$ and $\sin^2(\frac{\Delta}{2\hbar}t)$, respectively, where $\Delta/\hbar$ is the frequency of oscillations. Hence, the wave function is approximated by a macroscopic superposition of the states with $n=1$ and $n=0$ (Schrödinger cat state) as

$$|\Psi(t)\rangle \simeq \cos\left(\frac{\Delta}{2\hbar}t\right)|\Phi_1\rangle + i\sin\left(\frac{\Delta}{2\hbar}t\right)|\Phi_0\rangle. \tag{3}$$

In Fig. 2(b), we show the momentum occupations for $p=1,0,-1$, which behave almost identically to the overlaps, again justifying validity of the cat state description. We note that the similar cat state dynamics has been found also for quantum vortices in anisotropic traps[30] and supercurrents in two-color optical lattices.[31]

To measure the current oscillation in experiments, one has to be able to distinguish $|\Phi_0\rangle$ from $|\Phi_1\rangle$. It has been shown that this can be done by measuring the time-of-flight images.[31,32] In addition, the decoherence time has to be much larger than the period of the MQT oscillation. Since a cold atom system is completely isolated from an external thermal bath in contrast to normal condensed matter systems, the main source of the dissipation at zero temperature is the loss of atoms due to three-body recombination, which is neglected in the Bose-Hubbard Hamiltonian of Eq. (1). In a typical experiment of cold atoms in optical lattices,[17,33] the time scale of the three-body loss is on the order of 1s while the hopping time $\hbar/J$ in the superfluid regime is on the order of 100 μs. As seen in Fig. 2, the period of the MQT oscillation can be $\sim$10 ms ($100\hbar/J$), which is much smaller than the decoherence time, and thus there is a parameter region where the effect of the decoherence is safely negligible.

We next consider the case of $\theta_1=0$, where $|\Phi_1\rangle$ and $|\Phi_{-1}\rangle$ are degenerate. In this case, there are two possible scenarios of the fate of the supercurrent: (i) the supercurrent decays towards the zero-momentum state creating excitations. (ii) It coherently oscillates between $|\Phi_1\rangle$ and $|\Phi_{-1}\rangle$ as sketched in Fig. 1(b). Previous theoretical work on the supercurrent decay anticipated the first scenario to calculate the lifetime of the metastable state using the instanton method.[9,34,35] It is very likely that this scenario is indeed realized when the differences in winding numbers of θ_1 and θ_0 is large. In contrast, it is found in our numerical simulations that the second scenario mainly dictates the supercurrent dynamics as seen in Figs. 2(d) and 2(f). The supercurrent exhibits a coherent oscillation between states with velocities $v(t=0)$ and $-v(t=0)$ with rapid wiggles. If these wiggles are ignored, then the wave function is well approximated by superposition of the states $|\Phi_1\rangle$ and $|\Phi_{-1}\rangle$. The zero-momentum occupancy $n(p=0,t)$ (blue dashed line in Fig. 2) oscillates in time with the same frequency as the wiggles in the $n(p=\pm1,t)$ while the overlap of $|\Psi(t)\rangle$ with $|\Phi_0\rangle$ always remains zero. This means that the wiggles come from the coupling with the excited states with winding number 0 and that such states contribute to the wave function in addition to $|\Phi_1\rangle$ and $|\Phi_{-1}\rangle$.

Since during the coherent oscillations between the two degenerate states, the winding number changes from 1 to 0 (or to -1), one expects emergence of the phase slip associated with these oscillations. To reveal the phase slips, we calculate the time evolution of the average phase difference between the jth and $(j+r)$th sites, $\varphi(r,t)=\arg(\langle\hat{b}_j^\dagger\hat{b}_{j+r}\rangle)$. Notice that the phase difference is independent of j because of the homogeneity of the system. In Fig. 3, we show $\varphi(r,t)$ that corresponds to the dynamics depicted in Figs. 2(a)–2(c). At $t=0$ [Fig. 3(b)], $\varphi(r,t)$ linearly changes with r as $\varphi(r,t)=2\pi r/L$ corresponding to the winding number $n=1$. As time evolves, a phase kink develops around $r=L/2$ and it becomes $\sim\pi$ at $t=T/4$ [Fig. 3(c)]. Immediately after $t=T/4$, the phase jumps by 2π and the winding number changes to $n=0$ as seen in Fig. 3(d).

In Fig. 4, we show $\varphi(r,t)$ that corresponds to the situation shown in Fig. 2(d)–2(f), where the supercurrent oscillates between the states with $n=1$ and $n=-1$. As t increases, two phase kinks develop; which are localized around $r=L/4$ and $r=3L/4$. Both phase kinks are $\sim\pi$ at $t=T/4$ as shown in Fig. 4(c). When t exceeds $T/4$ [Fig. 4(d)], the phase jumps by 2π in the two regions $r\lesssim L/4$ and $r\gtrsim 3L/4$ so that the winding number changes to $n=-1$ by losing the phase of 4π in total. It is worth stressing that this "double phase slip" occurs without passing through a state with $n=0$ because the overlap of $|\Psi(t)\rangle$ with $|\Phi_0\rangle$ always remains zero during the oscillation.

We note that there is no direct connection between the phase slip in real time and that in imaginary time[34] (see also Sec. V). The dynamics in real time reflects the behavior of the average phase difference $\varphi(r,t)$, which comprises phase slips occurring at different times in different sites. This phase slip can be extracted from the superposition of two macroscopically distinct states with different winding numbers. At the same time the phase slip in imaginary time develops

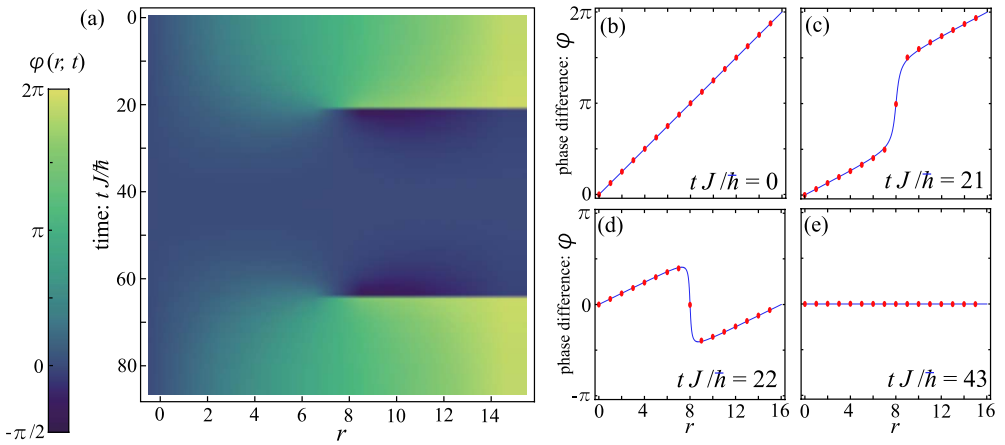

FIG. 3. (Color online) (a) Time evolution of the average phase difference $\varphi(r,t)$ for $L=N=16$, $U/J=2.5$, and $\theta_1=\pi/L$. The phase jumps by 2π at the boarders between the bright and dark regions. [(b)–(e)] Snap shots of $\varphi(r,t)$ for several values of t.

"instantaneously" during underbarrier tunneling in contrast to the phase kink in real time that exhibits a sinusoidal oscillation and develops gradually. Nevertheless the similarity between the shape of the phase slip in Figs. 3 and 4 and the expected shape of the kink in the instanton solution is very appealing.

In the above calculations, we took a relatively small system size $L=16$ and unit filling ($N=L$). To check that the basic properties of the supercurrent dynamics mentioned above do not change in a larger-sized system, we calculate the time evolution of the current velocity and the overlaps for $L=N=48$. In Figs. 5(a) and 5(b), we plot the current velocity $v(t)$ and the overlaps $|\langle\Phi_n|\Psi(t)\rangle|^2$ with $n=1,0,-1$ for $\theta_1=\pi/L$. These plots show that the coherent oscillation between the states with $n=1$ and $n=0$ occurs due to MQT also in this larger-sized system. In Figs. 5(c) and 5(d), we plot $v(t)$ and $|\langle\Phi_n|\Psi(t)\rangle|^2$ for $\theta_1=0$, which exhibits the coherent oscillation between the states $|\Phi_1\rangle$ and $|\Phi_{-1}\rangle$.

In Fig. 6, we show the frequency $\Delta/\hbar$ of the coherent oscillations as a function of L on a log-log scale. There we clearly see that the frequency monotonically decreases with L following a power law, $\Delta\propto L^{-\alpha}$, where α is a positive number monotonically decreasing with U/J. Since the current I at a fixed winding number is inversely proportional to L this implies that the frequency of oscillations scales as a power of the current. This effect is similar to the situation happening in two-dimensional superconductors at finite temperatures,[36] where the supercurrent dissipation rate coming from vortex unbinding also scales as a power of the current.

We also note that the commensurability of the filling factor is crucial for the coherent supercurrent dynamics. Only in case of commensurate fillings, the two states $|\Phi_1\rangle$ and $|\Phi_0\rangle$ (or $|\Phi_{-1}\rangle$) are coupled through the Umklapp-scattering process and the coherent oscillations can occur[26,27] (see Appendix A for a detailed explanation).

IV. MAPPING ONTO THE QUANTUM ROTOR MODEL

In the previous section, we have established from the exact TEBD simulations of the Bose-Hubbard model that the supercurrent dynamics exhibits coherent oscillations caused by MQT. For the comparison between the instanton and exact results, we need to calculate the energy splitting by means of the instanton method. In preparation for the instanton calculations of the energy splitting, in this section we

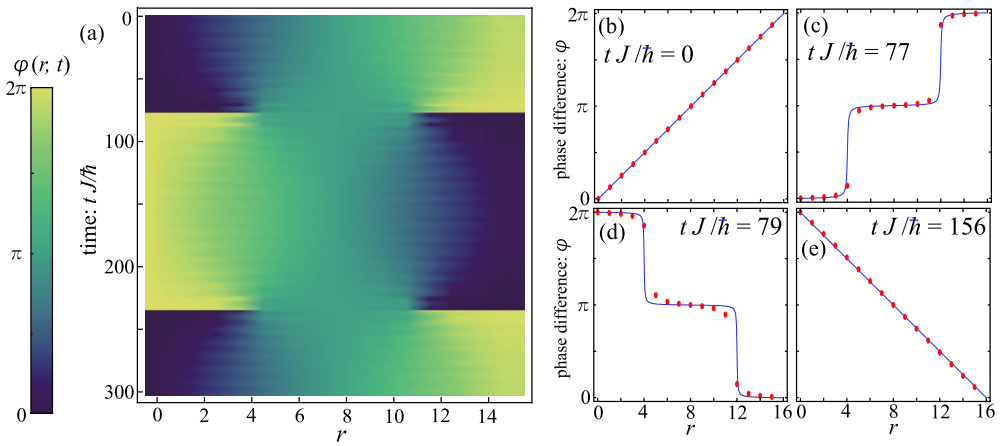

FIG. 4. (Color online) (a) Time evolution of the average phase difference $\varphi(r,t)$ for $L=N=16$, $U/J=2.5$, and $\phi_1=0$. [(b)–(e)] Snap shots of $\varphi(r,t)$ for several values of t.

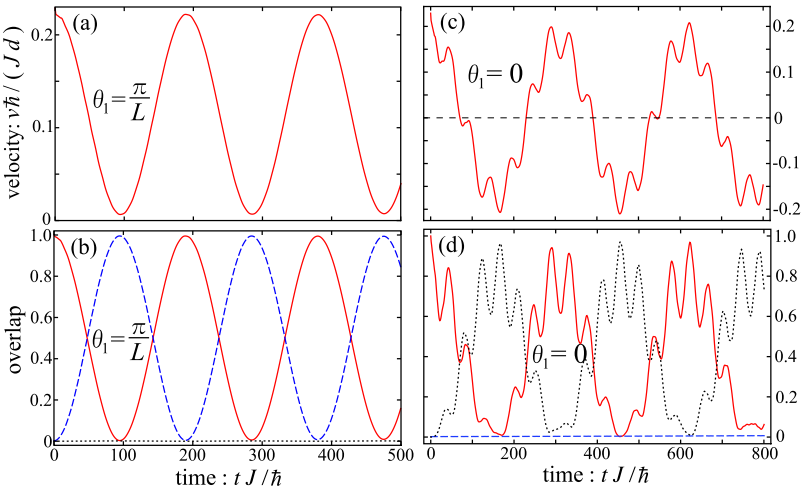

FIG. 5. (Color online) [(a) and (c)] Time evolution of the current velocity $v(t)$ and [(b) and (d)] the overlaps $|\langle\Phi_p|\Psi(t)\rangle|^2$. For $|\langle\Phi_p|\Psi(t)\rangle|^2$, the red solid, blue dashed, and black dotted lines correspond to $p=1$, 0, and -1. We set $L=N=48$ and $U/J=3$. In (a) and (b) $\theta_1=\pi/L$ while in (c) and (d) $\theta_1=0$.

explain the mapping of the Bose-Hubbard model onto the $O(2)$-quantum rotor model that is quantitatively valid when $U\nu \gg J$ and $\nu \gg 1$. While the qualitative properties of the supercurrent dynamics in the quantum rotor regime remain the same as in the case of $\nu=1$, this mapping allows us to obtain a simple analytical expression of the energy splitting as we will see in the following. Notice that the quantum rotor limit also describes a regular array of coupled Josephson junctions.[37]

We start with the grand canonical partition function,

$$Z=\int \mathcal{D}b^*\mathcal{D}b\,\exp\left\{-\frac{S[b^*,b]}{\hbar}\right\}, \tag{4}$$

where the action $S[b^*,b]$ for the Bose-Hubbard model is given by

$$S[b^*,b]=\sum_{j=1}^{L}\int_{-\hbar\beta/2}^{\hbar\beta/2}d\tau\Bigg[b_j^*(\tau)\hbar\frac{\partial}{\partial\tau}b_j(\tau)-J(b_j^*(\tau)b_{j+1}(\tau)e^{-i\theta}+b_{j+1}^*(\tau)b_j(\tau)e^{i\theta})+\frac{U}{2}b_j^*(\tau)b_j^*(\tau)b_j(\tau)b_j(\tau)-\mu b_j^*(\tau)b_j(\tau)\Bigg]. \tag{5}$$

Here, $\mu\approx U\nu$ is the chemical potential. For convenience we introduce finite small temperature T corresponding to the inverse temperature $\beta\equiv(k_BT)^{-1}$. In the end of calculations we will take the limit of $T\to 0$. Inserting $b_j=\sqrt{n_j}e^{i\phi_j}$, the action is rewritten as

$$S[n,\phi]=\sum_{j=1}^{L}\int_{-\hbar\beta/2}^{\hbar\beta/2}d\tau\Bigg[\hbar n_j\left(i\frac{\partial\phi_j}{\partial\tau}+\frac{1}{2n_j}\frac{\partial n_j}{\partial\tau}\right)-2\sqrt{n_jn_{j+1}}J\cos(\phi_{j+1}-\phi_j-\theta)+\frac{U}{2}(n_j-\nu)^2\Bigg]. \tag{6}$$

We split the number of particles per site into its average and fluctuation as $n_j=\nu+\delta n_j$, and assume that ν is integer and that $U\nu\gg J$ and $\nu\gg\delta n_j$. Then, we find that the action is approximated as

$$S[n,\phi]=\sum_{j=1}^{L}\int_{-\hbar\beta/2}^{\hbar\beta/2}d\tau\times\left[i\hbar\delta n_j\frac{\partial\phi_j}{\partial\tau}-2\nu J\cos(\phi_{j+1}-\phi_j-\theta)+\frac{U}{2}\delta n_j^2\right]. \tag{7}$$

Since Eq. (7) contains only the linear and quadratic terms with respect to number fluctuations δn_j, these degrees of freedom can be integrated out. Then, the action is described in terms of the phases as

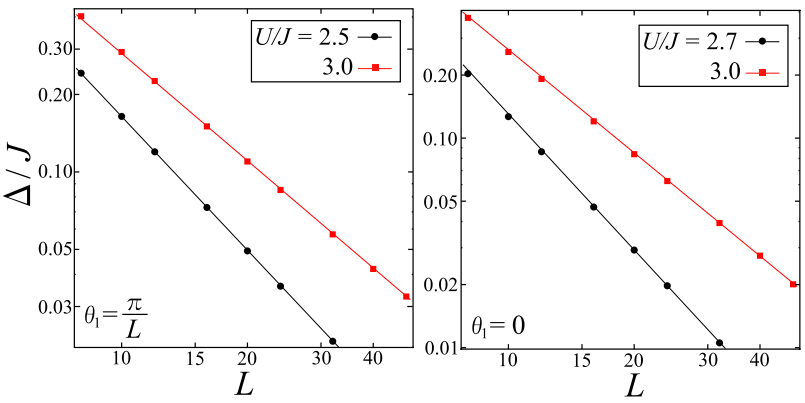

FIG. 6. (Color online) The frequencies Δ/J of the coherent oscillations versus the number of sites L for (a) $\theta_1=\pi/L$ and (b) $\theta_1=0$. The filling factor is fixed to be $\nu=1$. The plots are on a log-log scale.

$$S[\phi] = \sum_{j=1}^{L} \int_{-\hbar\beta/2}^{\hbar\beta/2} d\tau \left[\frac{\hbar^2}{2U} \left(\frac{\partial \phi_j}{\partial \tau} \right)^2 - 2\nu J \cos(\phi_{j+1} - \phi_j - \theta) \right]. \tag{8}$$

It is convenient to express the imaginary time in units of the Josephson plasma time $\hbar/E_{\mathrm{J}}$ as

$$\tau = \frac{\hbar}{E_{\mathrm{J}}} \tilde{\tau}, \tag{9}$$

where $E_{\mathrm{J}} \equiv \sqrt{\nu J U}$ is the Josephson plasma energy. Inserting Eq. (9) into Eq. (8), we obtain

$$S = \hbar \sqrt{\frac{\nu J}{U}} \tilde{s}, \tag{10}$$

where $\tilde{s}$ is the dimensionless action

$$\tilde{s}[\phi] = \sum_{j=1}^{L} \int_{-\tilde{\beta}/2}^{\tilde{\beta}/2} d\tilde{\tau} \left[\frac{1}{2} \left(\frac{d\phi_j}{d\tilde{\tau}} \right)^2 - 2 \cos(\phi_{j+1} - \phi_j - \theta) \right] \tag{11}$$

and $\tilde{\beta} = \beta E_{\mathrm{J}}$. From Eqs. (4) and (10) we clearly see that $h_{\mathrm{e}} \equiv \sqrt{U/(\nu J)}$ plays the role of the effective dimensionless Planck's constant for this problem. The limit of $h_{\mathrm{e}} \to 0$ corresponds to the classical (Bogoliubov) regime while at $h_{\mathrm{e}} \gtrsim 1$ quantum fluctuations become significant and can even drive the system to a different insulating phase.

Extremizing the action by imposing $\delta\tilde{s} = 0$, we obtain the classical equations of motion for the phases ϕ_j,

$$\frac{\partial^2 \phi_j}{\partial \tilde{\tau}^2} = 2 \sin(\phi_{j+1} - \phi_j - \theta) - 2 \sin(\phi_j - \phi_{j-1} - \theta). \tag{12}$$

There are two types of stationary solution of Eq. (12). One is

$$\phi_j = \frac{2\pi n}{L}(j-1) \tag{13}$$

which describes the current carrying states with the winding-number n. The other is a saddle-point solution with a phase kink separating (meta)stable states with different winding numbers

$$\phi_j = \frac{\alpha}{2} + \varphi(j-1), \tag{14}$$

where

$$\alpha = -\pi \frac{L-1+2n}{L-2} + 2\theta \frac{L-1}{L-2} \bmod 2\pi \tag{15}$$

and

$$\varphi = \frac{2\pi n - \alpha}{L-1}. \tag{16}$$

Notice that in Eq. (15) the phase kink is assumed to be located at the link between the first and Lth sites. The magnitude of this kink α is defined within the interval $[-2\pi, 0]$. In the limit of the large number of sites $L \gg 1$ the expression for α simplifies

$$\alpha \approx -\pi \left(1 + \frac{2n}{L} \right) + 2\theta \bmod 2\pi. \tag{17}$$

In particular, in the case $n=0$ and $\theta = \pi/L$, which we are interested in, $\alpha = -\pi(1-1/L) \approx -\pi$ and $\varphi = \pi/L$.

For $\theta = \pi/L$, the two current states with windings $n=1$ and $n=0$ are degenerate. Quantum tunneling couples them and breaks the degeneracy, leading to the energy splitting Δ between the ground (bonding) state and the first-excited (antibonding) state. This tunneling process is associated with generation of a "phase slip" or equivalently a phase kink. The virtual kink forms during the imaginary time evolution of the phase between the two current states. If the state of Eq. (13) with $n=1$ is prepared initially, the many-body wave function coherently oscillates with the frequency $\Delta/\hbar$ between the states with $n=1$ and $n=0$ as clearly observed in Fig. 2. It is well known[13] that the energy splitting can be expressed as

$$\Delta = 2 \lim_{\beta \to \infty} \frac{A}{\beta}, \tag{18}$$

where

$$A \equiv \frac{Z_1}{Z_0} \tag{19}$$

and

$$Z_1 = \int_{(1)} \mathcal{D}\phi \exp\left\{ -\frac{\tilde{s}[\phi]}{h_{\mathrm{e}}} \right\}, \quad Z_0 = \int_{(0)} \mathcal{D}\phi \exp\left\{ -\frac{\tilde{s}[\phi]}{h_{\mathrm{e}}} \right\}. \tag{20}$$

Notice that $\int_{(1)} \mathcal{D}\phi$ denotes the path integral over trajectories containing a single instanton while $\int_{(0)} \mathcal{D}\phi$ is the path integral containing zero instantons. According to the instanton method,[2,3] the energy splitting of Eq. (18) is well approximated by

$$\Delta \simeq 2LKE_{\mathrm{J}} \sqrt{\frac{\tilde{s}_I}{2\pi h_{\mathrm{e}}}} \exp\left(-\frac{\tilde{s}_I}{h_{\mathrm{e}}} \right), \tag{21}$$

where $\tilde{s}_I$ denotes the action for the instanton solution and K is the constant that we define below. Since the instanton method is a generalization of the WKB semiclassical approximation,[2,6] the expression for the energy splitting [Eq. (21)] is supposed to be accurate when $h_{\mathrm{e}}/\tilde{s}_I$ is sufficiently small. Note that in the right-hand side of Eq. (21), there is an additional factor of L. It reflects the fact that there are L independent instanton trajectories corresponding to the phase slip happening at one out of L links. The inclusion of this factor was *conjectured* by Callan and Coleman[3] but was never verified before. In the theory of thermal phase slip a similar factor was accurately derived from Langevin dynamics by McCumber and Halperin.[38] In Sec. VI we will show that this factor is indeed necessary to make the instanton method quantitatively accurate.

It is also worth stressing the advantage of the quantum rotor model that $\tilde{s}_I$ and K do not depend on ν and U/J but depend only on L. Thanks to this advantage, Δ/E_{J} depends on U, J, and ν only through h_{e}. In the following section we

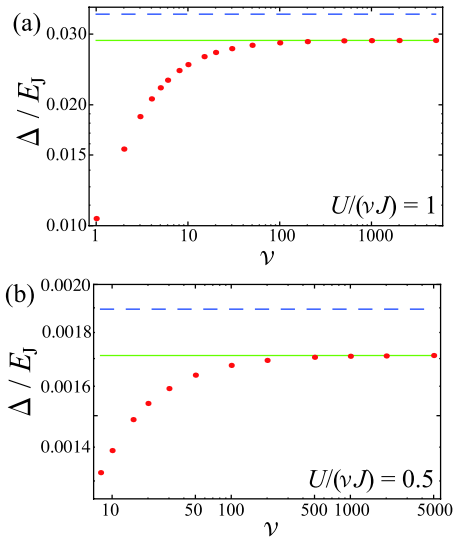

FIG. 7. (Color online) Ratio of the energy splitting Δ to the Josephson energy $E_J=\sqrt{\nu JU}$ as a function of ν for (a) $U/(\nu J)\equiv h_e^2=1$ and (b) $U/(\nu J)=0.5$. We set $L=8$. The dots are data obtained by using the TEBD method. The solid lines represent the value of Δ/E_J at $\nu=5000$. The dashed lines are the prediction of the instanton method. Notice that both U and ν are changed for a fixed value of J such that h_e remains constant.

will present a derivation of Eq. (21) first evaluating it approximately and then exactly and will give the explicit form of the coefficient K.

As mentioned above, the mapping onto the quantum rotor model is justified when $U\nu \gg J$ and $\nu \gg 1$. For unambiguous comparison between the TEBD and instanton results, we need to specify quantitatively the parameter region where the quantum rotor model is valid for the calculations of the energy splitting. It is clear in Eq. (21) that as ν increases at a fixed value of h_e, Δ/E_J should saturate at a constant corresponding to the quantum rotor limit. This is indeed the case as we show in Fig. 7, where we calculate Δ/E_J versus ν for $L=8$ and two different values of h_e with the use of the TEBD method (see Appendix B for the extension of TEBD to the case of large filling factors). Note that this ratio Δ/E_J becomes independent on ν only at very large filling factors $\nu \gtrsim 1000$. We also want to point out that for the smaller value of h_e the larger the filling factor is required to be for the convergence. Since our quantitative analysis is focused on the region of $U/(\nu J)\gtrsim 0.5$, the quantum rotor model is sufficiently accurate for $\nu=1000$, which we use in practice.

V. INSTANTON METHOD FOR THE QUANTUM ROTOR MODEL

A. One collective variable

Since the instanton method in the presence of many degrees of freedom is quite complicated, we first use a simpler model, which is reduced from the quantum rotor model by assuming that the phase slip is described by only a single collective variable. This simple model, which represents a variational estimate of the full result, is useful to understand

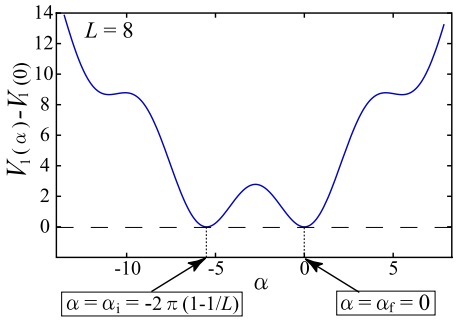

FIG. 8. (Color online) Effective potential $V_1(\alpha)$ for $\theta=\pi/L$ and $L=8$.

basic ideas of the calculation. Later we will generalize the result to the phase slip described by two degrees of freedom and finally show the complete instanton solution of the full problem. In the regime of validity of the quantum rotor model, the healing length $\xi=d\sqrt{2J/(\nu U)}$ is much shorter than the lattice spacing d. Hence the phase slip that develops during the tunneling process should be localized within a few sites. Without loss of generality, we can assume that the phase kink develops at the link between the first and Lth sites. In the first approximation we assume that the phases along the instanton trajectory satisfy the ansatz,

$$\phi_j(\tilde{\tau}) = \frac{\alpha(\tilde{\tau})}{2} + \varphi(\tilde{\tau})(j-1), \tag{22}$$

where α denotes the phase difference between the first and Lth sites. Its time dependence is found from extremizing the effective action (see below). The remaining phases on other sites are chosen as a simple linear function of the site index j with $\varphi\equiv-\alpha/(L-1)$ such that the boundary condition $\phi_L=-\alpha/2$ is fulfilled. Substituting Eq. (22) into Eq. (11) we find that the effective dimensionless action describing the system becomes

$$\tilde{s}[\alpha] = \int d\tilde{\tau}\left[\frac{M}{2}\left(\frac{\partial\alpha}{\partial\tilde{\tau}}\right)^2 + V_1(\alpha)\right]. \tag{23}$$

This is nothing but the classical action of a particle with the effective mass M, which depends on the system size according to

$$M = \frac{L(L+1)}{12(L-1)}, \tag{24}$$

moving in the effective potential $-V_1(\alpha)$, where

$$V_1(\alpha) = -2\cos(\alpha-\theta) - 2(L-1)\cos(\varphi-\theta). \tag{25}$$

The shape of $V_1(\alpha)-V_1(0)$ for $\theta=\pi/L$ and $L=8$ is depicted in Fig. 8. $V_1(\alpha)$ has two global minima $\alpha=\alpha_i\equiv-2\pi(1-1/L)$ and $\alpha=\alpha_f\equiv 0$ corresponding to the current-carrying states with winding numbers $n=1$ and $n=0$, respectively. These two minima are separated by a local maximum, $\alpha=\alpha_s\equiv-\pi(1-1/L)$ describing the saddle-point solution of Eq. (15). Thus, introducing the collective variable α, the phase slip problem is equivalent to tunneling of a single particle in a one-dimensional symmetric double-well

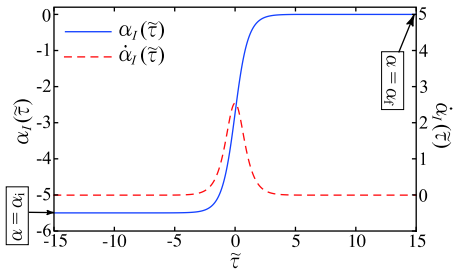

FIG. 9. (Color online) Instanton solution $\alpha_I(\tilde{\tau})$ and $\partial_{\tilde{\tau}}\alpha_I(\tilde{\tau})$.

potential. The corresponding classical equation of motion describing the particle motion in the (inverted) potential $-V_1(\alpha)$ is

$$-M\frac{\partial^2\alpha}{\partial\tau^2}+\frac{\partial V_1}{\partial\alpha}=0. \tag{26}$$

The instanton solution of this equation $\alpha(\tilde{\tau})=\alpha_I(\tilde{\tau})$ is the one satisfying the boundary conditions $\alpha(-\tilde{\beta}/2)=\alpha_i$ and $\alpha(\tilde{\beta}/2)=\alpha_f$. Such a solution (shown in Fig. 9) contains a kink in the phase α. The instanton solution defines the classical trajectory in the path integral of Z_1. There is another trivial solution of Eq. (26), $\alpha(\tilde{\tau})=\alpha_i$ [or equivalently $\alpha(\tilde{\tau})=\alpha_f$], which is the classical trajectory corresponding to the path integral of Z_0.

To calculate the ratio A in Eq. (19) (see Ref. 6 for more details), we substitute

$$\alpha(\tilde{\tau})=\alpha_I(\tilde{\tau})+\sqrt{\frac{h_e}{M}}\sum_m c_m\xi_m(\tilde{\tau}), \tag{27}$$

into Z_1 and

$$\alpha(\tilde{\tau})=\alpha_i+\sqrt{\frac{h_e}{M}}\sum_m c_m\xi_m^{(0)}(\tilde{\tau}), \tag{28}$$

into Z_0, where ξ_m's and $\xi_m^{(0)}$'s are complete sets of real orthonormal functions obeying the following eigenvalue equations:

$$\left(-\frac{\partial^2}{\partial\tilde{\tau}^2}+\frac{1}{M}\left.\frac{\partial^2V_1}{\partial\alpha^2}\right|_{\alpha=\alpha_{cl}}\right)\xi_m(\tilde{\tau})=\lambda_m\xi_m(\tilde{\tau}) \tag{29}$$

and

$$\left(-\frac{\partial^2}{\partial\tilde{\tau}^2}+\omega^2\right)\xi_m^{(0)}(\tilde{\tau})=\lambda_m^{(0)}\xi_m^{(0)}(\tilde{\tau}) \tag{30}$$

with $\omega^2=M^{-1}\partial_\alpha^2V_1|_{\alpha=\alpha_i}$. Neglecting the terms higher than the second order with respect to $\sqrt{h_e/M}$, A is approximated as

$$A\simeq\exp\left(-\frac{\tilde{s}_I}{h_e}\right)\times\frac{\int\cdots\int\prod_m(2\pi)^{-1/2}dc_m\exp\left[-\frac{1}{2}\sum_m\lambda_mc_m^2\right]}{\int\cdots\int\prod_m(2\pi)^{-1/2}dc_m\exp\left[-\frac{1}{2}\sum_m\lambda_m^{(0)}c_m^2\right]}, \tag{31}$$

where $\tilde{s}_I$ is the action of the instanton solution given by

$$\tilde{s}_I=\int d\tilde{\tau}M\left(\frac{\partial\alpha_I}{\partial\tilde{\tau}}\right)^2. \tag{32}$$

Notice that the neglect of the higher order terms with respect to h_e is the main source of the error in the instanton method and this is the reason why the instanton method can provide a quantitatively correct value of the energy splitting only in the semiclasical limit, $h_e/s_I\ll1$.

To carry out the integrals with respect to c_m's in Eq. (31), it is important that due to the translation invariance of the instanton solution in the imaginary time, Eq. (29) possesses one solution ξ_0 with the eigenvalue $\lambda_0=0$. For this zero mode, the integral in Eq. (31) is formally divergent. To solve this problem, one needs simply replace $\int dc_0$ with $\sqrt{\tilde{s}_I/h_e}\int d\tilde{\tau}$ leading to

$$A=\beta\sqrt{\nu JU}\left(\frac{\prod_m\lambda_m^{(0)}}{\prod_{m\neq0}\lambda_m}\right)^{1/2}\sqrt{\frac{\tilde{s}_I}{2\pi h_e}}\exp\left(-\frac{\tilde{s}_I}{h_e}\right). \tag{33}$$

In the above discussion, we assumed that the phase kink develops at the link between the first and Lth sites. In total there are L-independent possibilities for the kink. Note that because we are dealing with a discrete system, there is no continuous symmetry associated with this degeneracy and thus no additional zero eigenvalue in Eq. (33). All instanton solutions centered around different links give identical contribution to Z_1. It is therefore only necessary to multiply A by L before substituting it into Eq. (18). Thus, we obtain Eq. (21) with the coefficient

$$K=\left(\frac{\prod_m\lambda_m^{(0)}}{\prod_{m\neq0}\lambda_m}\right)^{1/2}. \tag{34}$$

Now both s_I and K can be straightforwardly found numerically. In the case of a single collective variable described here, s_I and K for $L=8$ are explicitly given in the first row of Table I.

B. Two collective variables

After considering a toy single-variable approximation to the instanton solution, in this section, we make the next step by increasing the total number of the collective variables to two. Specifically to describe the instanton action we take two variables α and β describing the phase slip as independent and use the linear interpolating function for the rest. The

TABLE I. $\tilde{s}_I$ and K for several values of the number of collective variables, where $L=8$.

Number of collective valiables: m	Instanton action: $\tilde{s}_I$	Coefficient: K
1	7.749	3.71
2	7.396	4.89
3	7.364	4.41
4	7.363	3.64
8	7.363	3.06

phases of such instanton solution (again centered between first and Lth sites) are described as

$$\phi_j(\tilde{\tau}) = \begin{cases} \alpha(\tilde{\tau})/2, & \text{for} \quad j=1 \\ \alpha(\tilde{\tau})/2 + \beta(\tau) + \varphi(\tilde{\tau})(j-2), & \text{for} \quad 2 \le j \le L-1 \\ -\alpha(\tilde{\tau})/2, & \text{for} \quad j=L \end{cases}, \tag{35}$$

where α denotes the phase difference between the first and Lth sites, β is the phase difference between the second and first [as well as Lth and $(L-1)$th] sites, and $\varphi \equiv -(\alpha+2\beta)/(L-3)$ is chosen such that the boundary condition $\phi_{L-1}=-\phi_2$ is fulfilled. Substituting Eq. (35) into Eq. (11) we find that the action is described by the two variables α and β as

$$\tilde{s}[\alpha,\beta] = \int d\tilde{\tau}\left[\frac{1}{2}C_{11}\left(\frac{\partial\alpha}{\partial\tilde{\tau}}\right)^2 + C_{12}\frac{\partial\alpha}{\partial\tilde{\tau}}\frac{\partial\beta}{\partial\tilde{\tau}} + \frac{1}{2}C_{22}\left(\frac{\partial\beta}{\partial\tilde{\tau}}\right)^2 + V_2(\alpha,\beta)\right], \tag{36}$$

where

$$C_{11} = \frac{L^2+3L+16}{12(L-3)}, \quad C_{22} = 2C_{12} = \frac{(L-1)(L-2)}{3(L-3)}, \tag{37}$$

and $V_2(\alpha,\beta)$ is the following effective potential:

$$V_2(\alpha,\beta) = -2\cos(\alpha-\theta) - 4\cos(\beta-\theta) - 2(L-3)\cos(\varphi-\theta). \tag{38}$$

It is convenient to perform a linear transformation $(x,y)^{\mathbf{t}}=\hat{X}(\alpha,\beta)^{\mathbf{t}}$, where $\hat{X}$ is an orthogonal 2×2 matrix, to diagonalize the kinetic energy part of the action leading to

$$\tilde{s}[x,y] = \int d\tilde{\tau}\left[\frac{1}{2}M_x\left(\frac{\partial x}{\partial\tilde{\tau}}\right)^2 + \frac{1}{2}M_y\left(\frac{\partial y}{\partial\tilde{\tau}}\right)^2 + V_2(x,y)\right]. \tag{39}$$

The shape of $V_2(x,y)-V_2(0,0)$ for $\theta=\pi/L$ and $L=8$ is depicted in Fig. 10. In the potential there are two minima corresponding to the current states with $n=0$ and $n=1$. The classical equations of motion corresponding to this action are

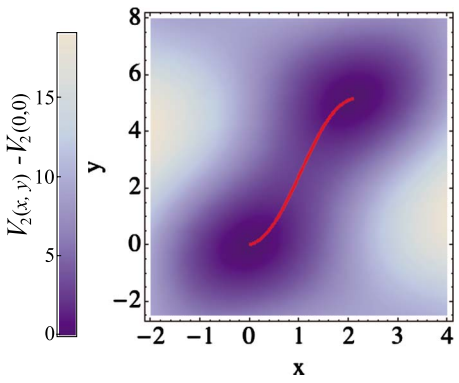

FIG. 10. (Color online) Effective potential $V_2(x,y)-V_2(0,0)$ for $\theta=\pi/L$ and $L=8$. The solid line represents the trajectory of the instanton solution.

$$-M_x\frac{\partial^2 x}{\partial\tau^2} + \frac{\partial V_2}{\partial x} = 0,$$

$$-M_y\frac{\partial^2 y}{\partial\tau^2} + \frac{\partial V_2}{\partial y} = 0. \tag{40}$$

As in the case of the single collective variable, the instanton solution describes the classical trajectory in the inverted potential, which starts from one of the maxima of $-V_2(x,y)$ [or equivalently minima of $V_2(x,y)$] at $-\tilde{\tau}=\tilde{\beta}/2$ and reaches the other maximum at $\tilde{\tau}=\tilde{\beta}/2$ through a saddle point as shown in Fig. 11. The trajectory of the instanton solution is indicated by the solid line in Fig. 10. Inserting the instanton solution into Eq. (39), we obtain $\tilde{s}_I$. The derivation of the coefficient K in Eq. (21) is almost the same as that for the single collective variable and we skip it to avoid redundancy. The values of both $\tilde{s}_I$ and K for $L=8$ in this two-variable case can be found in the second line of Table I. In a similar way one can keep on the number of independent degrees of freedom in the instanton solution.

C. All degrees of freedom

As a final step we will explicitly show generalization of the instanton method to the action of the quantum rotor model Eq. (11) where all phases are treated as independent variable. We will show that the energy splitting is given by Eq. (33) where the eigenvalue Eqs. (29) and (30) are appro-

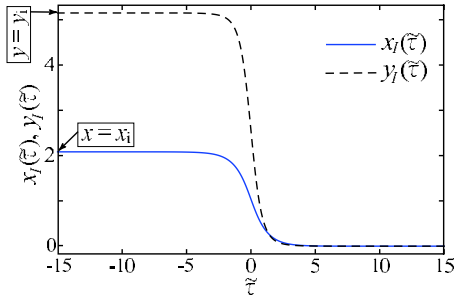

FIG. 11. (Color online) Instanton solution $x_I(\tilde{\tau})$ and $y_I(\tilde{\tau})$ for $\theta=\pi/L$ and $L=8$.

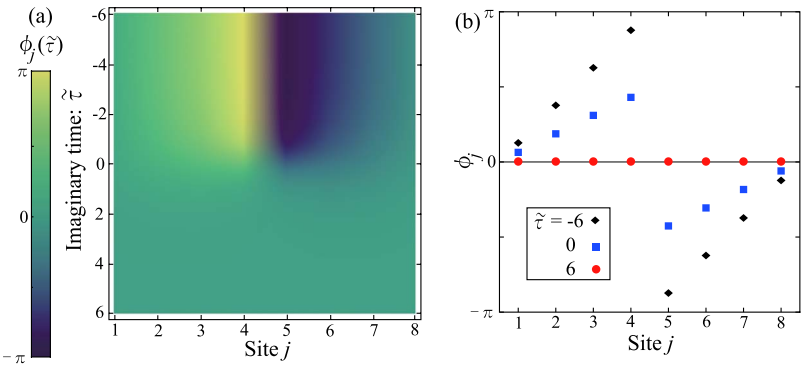

FIG. 12. (Color online) (a) Instanton solution $\vec{\phi}_I(\tilde{\tau})$ for $\theta=\pi/L$ and $L=8$. (b) Snap shots of $\vec{\phi}_I(\tilde{\tau})$ for $\tilde{\tau}=-6$ (black diamonds), 0 (blue squares), and 6 (red circles).

priately generalized. For convenience, we rewrite Eq. (11) as

$$\tilde{s}=\int d\tilde{\tau}\left[\frac{1}{2}\frac{\partial\vec{\phi}}{\partial\tilde{\tau}}\cdot\frac{\partial\vec{\phi}}{\partial\tilde{\tau}}+V(\vec{\phi})\right], \tag{41}$$

where $\vec{\phi}$ is an L-dimensional vector defined as

$$\vec{\phi}=[\phi_1(\tilde{\tau}),\ldots,\phi_j(\tilde{\tau}),\ldots,\phi_L(\tilde{\tau})]^{\mathbf{t}} \tag{42}$$

and the potential is

$$V(\vec{\phi})=\sum_{j=1}^{L}V_j(\phi_{j+1},\phi_j)=\sum_{j=1}^{L}-2\cos(\phi_{j+1}-\phi_j-\theta). \tag{43}$$

The classical equations of motion Eq. (12) have an instanton solution $\vec{\phi}(\tilde{\tau})=\vec{\phi}_I(\tilde{\tau})$ that connects two current states through the saddle point having a phase kink. We obtain such a solution by numerically solving Eq. (12) imposing the boundary conditions

$$\phi_j(-\tilde{\beta}/2)=\frac{2\pi j}{L}-\pi\left(1+\frac{1}{L}\right),\quad \phi_j(\tilde{\beta}/2)=0. \tag{44}$$

The corresponding instanton solution for $L=8$ is depicted in Fig. 12. Notice that apart from the kink between fourth and fifth sites the remaining phases approximately linearly depend on the site index justifying the single-variable variational ansatz made in Sec. V A. However, because of high sensitivity of the splitting Δ to especially the value of $\tilde{s}$ such ansatz can not be used for accurate quantitative calculations. We intentionally shifted the position of the kink in Fig. 12 to the middle of the system for better graphical presentation. For computational purposes it is convenient to assume that the link develops between first and Lth sites as we did in earlier calculations. Substituting $\vec{\phi}(\tilde{\tau})=\vec{\phi}_I(\tilde{\tau})$ into Eq. (41), we obtain the instanton action $\tilde{s}_I$.

To calculate A of Eq. (19), we substitute

$$\vec{\phi}(\tilde{\tau})=\vec{\phi}_I(\tilde{\tau})+\sqrt{h_e}\sum_m c_m\vec{\xi}_m(\tilde{\tau}) \tag{45}$$

into Z_1 and

$$\vec{\phi}(\tilde{\tau})=\vec{\phi}(-\tilde{\beta}/2)+\sqrt{h_e}\sum_m c_m\vec{\xi}_m^{(0)}(\tilde{\tau}) \tag{46}$$

into Z_0, where

$$\vec{\xi}_m=[\xi_{1,m}(\tilde{\tau}),\ldots,\xi_{j,m}(\tilde{\tau}),\ldots,\xi_{L,m}(\tilde{\tau})]^{\mathbf{t}}, \tag{47}$$

$$\vec{\xi}_m^{(0)}=[\xi_{1,m}^{(0)}(\tilde{\tau}),\ldots,\xi_{j,m}^{(0)}(\tilde{\tau}),\ldots,\xi_{L,m}^{(0)}(\tilde{\tau})]^{\mathbf{t}}. \tag{48}$$

The L-dimensional vectors $\vec{\xi}_m$'s and $\vec{\xi}_m^{(0)}$'s obey the eigenvalue equations

$$\hat{\mathcal{M}}\vec{\xi}_m(\tilde{\tau})=\lambda_m\vec{\xi}_m(\tilde{\tau}), \tag{49}$$

$$\hat{\mathcal{M}}^{(0)}\vec{\xi}_m^{(0)}(\tilde{\tau})=\lambda_m^{(0)}\vec{\xi}_m^{(0)}(\tilde{\tau}), \tag{50}$$

and the orthonormalization conditions

$$\int d\tilde{\tau}\vec{\xi}_l\cdot\vec{\xi}_m=\delta_{l,m},\quad \int d\tilde{\tau}\vec{\xi}_l^{(0)}\cdot\vec{\xi}_m^{(0)}=\delta_{l,m}. \tag{51}$$

The $L\times L$-dimensional matrices $\hat{\mathcal{M}}$ and $\hat{\mathcal{M}}^{(0)}$ are determined by the matrix elements

$$\mathcal{M}_{j,k}=\delta_{j,k}\left(-\frac{\partial^2}{\partial\tau^2}+\left.\frac{\partial^2V_j}{\partial\phi_j^2}\right|_{\vec{\phi}=\vec{\phi}^I}+\left.\frac{\partial^2V_{j-1}}{\partial\phi_j^2}\right|_{\vec{\phi}=\vec{\phi}^I}\right)+\delta_{j,k-1}\left.\frac{\partial^2V_j}{\partial\phi_j\,\partial\,\phi_{j+1}}\right|_{\vec{\phi}=\vec{\phi}^I}+\delta_{j,k+1}\left.\frac{\partial^2V_{j-1}}{\partial\phi_j\,\partial\,\phi_{j-1}}\right|_{\vec{\phi}=\vec{\phi}^I}, \tag{52}$$

$$\mathcal{M}_{j,k}^{(0)}=\delta_{j,k}\left(-\frac{\partial^2}{\partial\tau^2}+2\omega^2\right)-\delta_{j,k-1}\omega^2-\delta_{j,k+1}\omega^2, \tag{53}$$

where $\omega^2=\partial_{\phi_j}^2V_j|_{\vec{\phi}=\vec{0}}$. Notice that $(L+1)$th and zeroth sites are equivalent to first and Lth sites, respectively, reflecting the periodicity of the system. Neglecting the terms higher than the second order with respect to $\sqrt{h_e}$, A is again approximated as Eq. (31). The derivation of Eq. (21) with the coefficient K given by Eq. (34) is exactly the same as the case of the single collective variable and will not be repeated here. The only difference with the single variable case is that λ_m's and $\lambda_m^{(0)}$'s are now given by the eigenvalues of Eqs. (49) and (50). For $L=8$, we obtain $\tilde{s}_I=7.363$ and $K=3.06$ as explicitly given in Table I.

VI. COMPARISON BETWEEN THE INSTANTON AND EXACT RESULTS

We now compare the frequency of oscillations calculated by the instanton method with the TEBD results. We choose the situation of $\theta_1=\pi/L$ and $L=8$, characterized by a single

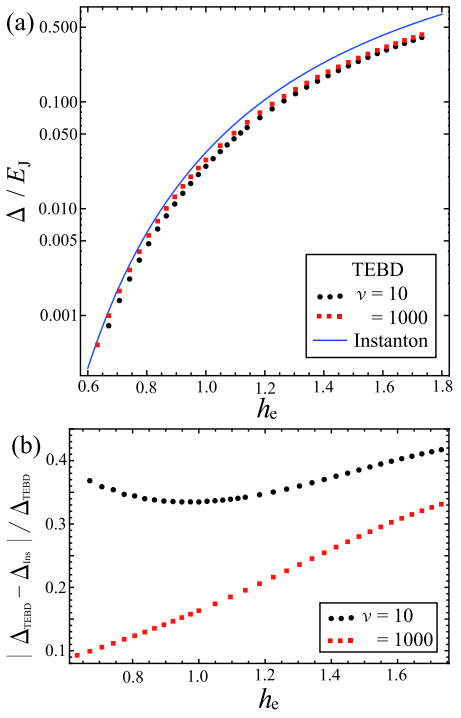

FIG. 13. (Color online) (a) Energy splitting Δ/E_J as a function of the effective Planck's constant $h_e \equiv \sqrt{U/(\nu J)}$ for $L=8$. The blue solid line represents the result by the instanton method corresponding to Eq. (21) with $\tilde{s}_I=7.363$ and $K=3.06$. The red squares and the black circles are the TEBD results for $\nu=1000$ and $\nu=10$, respectively. (b) Ratio $|\Delta_{\mathrm{TEBD}}-\Delta_{\mathrm{Ins}}|/\Delta_{\mathrm{TEBD}}$ of the difference between the TEBD and instanton results as a function of h_e.

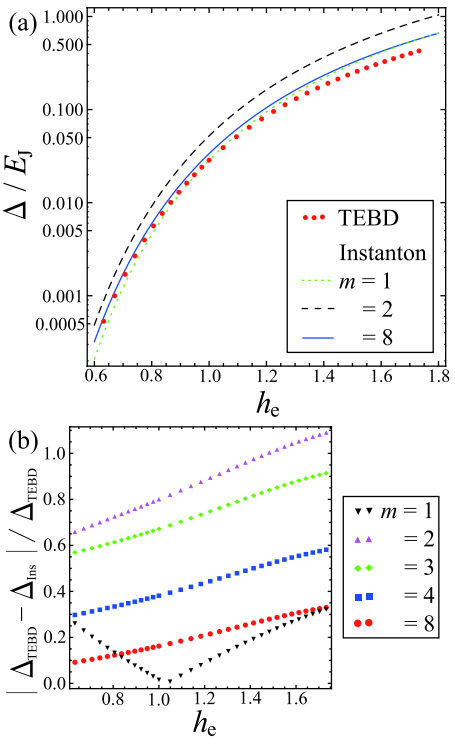

FIG. 14. (Color online) (a) Energy splitting Δ/E_J versus the effective Planck's constant $h_e \equiv \sqrt{U/(\nu J)}$. The dotted, dashed, and solid lines represent the results by the instanton method for $m=1$, 2, and 8. The dots are the TEBD results for $\nu=1000$. (b) Ratio $|\Delta_{\mathrm{TEBD}}-\Delta_{\mathrm{Ins}}|/\Delta_{\mathrm{Ins}}$ of the difference between the TEBD and instanton results as a function of h_e.

phase slip dynamics. We can extract the energy splitting Δ from TEBD simulations by fitting the overlap $|\langle\Phi_1|\Psi(t)\rangle|^2$ [like in Fig. 2(c)] using the function

$$f(t) = B\cos^2\left(\frac{\Delta}{2\hbar}t\right) + C, \tag{54}$$

where Δ, B, and C are the free parameters. In Fig. 13(a), we show the energy splitting Δ versus h_e calculated by the instanton method (blue solid line), and by TEBD for the filling factors $\nu=1000$ (red squares) and $\nu=10$ (black circles). We recall that how to apply TEBD to the Bose-Hubbard system with large filling factors is explained in detail in Appendix B. It is evident that for $\nu=1000$ and h_e sufficiently small the instanton and TEBD results agree very well. To quantify the error of the instanton method, in Fig. 13(b) we show the relative difference between the two results: $|\Delta_{\mathrm{TEBD}}-\Delta_{\mathrm{Ins}}|/\Delta_{\mathrm{TEBD}}$. For $\nu=1000$ (red squares), as h_e decreases, the error also decreases such that it is within 10% when $h_e \lesssim 0.7$. It is hard to push the calculation to even smaller values of h_e because of exponential sensitivity of the frequency of oscillations to the effective Planck's constant. Nevertheless our results allow us to make the conclusion that the instanton method can provide quantitatively accurate prediction for the tunneling probability when $h_e/\tilde{s}_I$ is sufficiently small. At the same time, the error for $\nu=10$ is significantly larger than that for $\nu=1000$. Moreover the error does not even monotonically depend on h_e. This clearly means that at this filling the quantum rotor model gives only qualitative description of the tunneling process.

It is also instructive to learn how the instanton method is improved as the number of collective variables increases. To see this, let us now present the comparison between the TEBD and the approximate instanton results where only $m<L$ collective variables are treated as independent. We take $L=8$ again. In Table I, we show the instanton action $\tilde{s}_I$ and the coefficient K for several values of m. Both $\tilde{s}_I$ and K approach the exact values corresponding to $m=8$ as m increases. We note that the action $\tilde{s}_I$ for $m=4$ is exactly the same as that for $m=8$ because the instanton solution is antisymmetric with respect to $j \to L-j$, i.e., with respect to the link at which the phase kink develops (see Fig. 12). In contrast, K for $m=4$, where the fluctuations are also forced to obey the same symmetry as well, is significantly different from K for $m=8$. Thus, it is crucial to include all possible fluctuations in order to obtain the correct value of K.

In Fig. 14(a), we plot the energy splitting calculated by the instanton method as a function of h_e together with that by TEBD for $\nu=1000$. At first glance, it seems that the results by the instanton method with a single collective variable agrees very well with the TEBD results. However, this seeming agreement is rather coincidental as shown in Fig. 14, where we plot the ratio $|\Delta_{\mathrm{TEBD}}-\Delta_{\mathrm{Ins}}|/\Delta_{\mathrm{Ins}}$ of the difference between the energy splittings by TEBD, Δ_{TEBD}, and the instanton method, Δ_{Ins}. There we clearly see that the error for $m=1$ (black triangles) does not monotonically decrease with

h_e, contradicting the basic fact that the instantons should be more accurate at smaller h_e. Except for this case with $m=1$, the error decreases monotonically as the number of independent phases m increases and the effective Planck's constant h_e decreases.

VII. CONCLUSION

We analyzed quantum dynamics of supercurrents of one-dimensional lattice bosons in a ring. In particular, our focus was on the coherent oscillations between the two degenerate current states via macroscopic quantum tunneling (MQT). We calculated the energy splitting Δ both simulating real-time dynamics using the time-evolving block decimation (TEBD) method and within the imaginary-time instanton method. We showed that the result of instanton calculation is in very good quantitative agreement with the TEBD result when the effective Planck's constant h_e is sufficiently small. This agreement verifies the instanton method applied to coherent MQT involving many collective variables.

We also want to emphasize that the success in applying TEBD (or equivalently the time-dependent density matrix renormalization group) to MQT problems opens up new possibilities to analyzing macroscopic-tunneling phenomena. In particular, (i) TEBD allows us to precisely calculate the energy splitting even for large h_e, where the instanton method fails. (ii) TEBD provides time evolution of the many-body wave function, from which one can calculate various quantities, for example different correlation functions. The first advantage is crucial for quantitative simulation of experiments (e.g., in cold gases), where it is easier to work in the regime of larger h_e and shorter periods to avoid various effects of decoherence like particle losses. Moreover, the second advantage allows one to reveal detailed processes of MQT in real time. As an example, we have analyzed the time evolution of the phase-phase correlation functions and revealed the existence of the phase slips associated with the coherent oscillations, which can be detected in experiments. One can extend this analysis to study higher order correlation functions to, e.g., detect shot noise of phase slips or even their full counting statistics.[39]

Note added. On the same day when the present paper was posted on arXiv, a relevant study on supercurrent dynamics in infinite-size 1D lattice bosons appeared.[40]

ACKNOWLEDGMENTS

The authors thank E. Altman, Y. Kato, S. Kurihara, T. Nikuni, M. Nishida, and A. Nunnenkamp for valuable comments and discussions. I.D. acknowledges support from a Grant-in-Aid from JSPS. I.D. is grateful to Boston University visitors program for hospitality. A.P. was supported by AFOSR under Grant No. FA9550-10-1-0110 and Sloan Foundation.

APPENDIX A: ORIGIN OF THE TUNNELING COUPLING BETWEEN THE TWO CURRENT STATES

While in Sec. IV we described the tunneling between the two current states in terms of the phase slips, it will be helpful to explain directly from the Bose-Hubbard model that the origin of the tunneling is the Umklapp-scattering process. For this purpose, we briefly review the analyses previously made by Refs. 26 and 27.

Substituting the Fourier transform of the bosonic field operator,

$$\hat{b}_j = \frac{1}{\sqrt{L}} \sum_{q=0}^{L-1} \hat{\beta}_q e^{i2\pi qj/L} \tag{A1}$$

into Eq. (1), we rewrite the Bose-Hubbard Hamiltonian in the quasimomentum representation,

$$\hat{H} = \sum_{q=0}^{L-1} \varepsilon_q \hat{\beta}_q^\dagger \hat{\beta}_q + \frac{U}{2L} \sum_{q_1,q_2,q_3} \hat{\beta}_{q_1}^\dagger \hat{\beta}_{q_2}^\dagger \hat{\beta}_{q_3} \hat{\beta}_{\|q_1+q_2-q_3\|_L} \tag{A2}$$

where $\varepsilon_q = -2J\cos(2\pi q/L-\theta)$ is the single-particle energy and the notation $\|\ \|_L$ denotes modulo L. The modulus is specific to a lattice system, where the quasimomentum increases by an integer multiple of the reciprocal lattice vector $2\pi/d$ in a scattering process (the Umklapp process).

For simplicity, we first consider the noninteracting case, $U=0$. When $\theta=\pi/L$, the single-particle energies for $q=0$ and $q=1$ are degenerate. This means that when there are N particles in the system, the ground state is $(N+1)$ fold degenerate, and we represent the $N+1$ degenerate states as $|N_0,N-N_0\rangle$, where N_0 particles occupy the $q=0$ state and $N-N_0$ particles occupy the $q=1$ state.

The onsite interaction breaks the degeneracy. To show this, assuming $\nu U \ll J$, we treat the onsite interaction term $\hat{V} \equiv U/(2L)\Sigma_{q_1,q_2,q_3} \hat{\beta}_{q_1}^\dagger \hat{\beta}_{q_2}^\dagger \hat{\beta}_{q_3} \hat{\beta}_{\|q_1+q_2-q_3\|_L}$ as a perturbation. Since there is no direct coupling between the different $|N_0,N-N_0\rangle$ states, the energy in the first-order perturbation is given by

$$E^{(1)} = N\varepsilon_0 + \langle N-N_0,N_0|\hat{V}|N-N_0,N_0\rangle \tag{A3}$$

$$= N\varepsilon_0 + \frac{U}{2L}[N(N-1)+2N_0(N-N_0)]. \tag{A4}$$

From Eq. (A4) we see that there are two states with the minimal energy, which are $|N,0\rangle$ and $|0,N\rangle$. The onsite interaction breaks the degeneracy of $|N,0\rangle$ and $|0,N\rangle$ only in the case of commensurate fillings ($\|N\|_L=0$).[26,27] This is because in the commensurate case the total quasimomentum, $P=2\pi/(Ld)\|\Sigma_{q=0}^{L-1} q\langle\hat{\beta}_q^\dagger\hat{\beta}_q\rangle\|_L$, of the $|N,0\rangle$ state is equal to that of the $|0,N\rangle$ state and therefore the onsite interaction couples these two states through a multiple Umklapp process. This coupling leads to a finite energy splitting Δ between the ground state, $2^{-1/2}(|N,0\rangle+|0,N\rangle)$, and the first excited state, $2^{-1/2}(|N,0\rangle-|0,N\rangle)$. Contrary, in the incommensurate case, the two states have different total quasimomenta and the degeneracy is not broken.

To confirm the scenario mentioned above, we show the twelve lowest energy levels versus θL in Fig. 15, which were calculated by the exact diagonalization of Eq. (1) with $L=N=8$. In Fig. 15(a), where $U=0$, $|N,0\rangle$, and $|0,N\rangle$ are degenerate at $\theta=\pi/L$ as indicated by the arrow. In the pres-

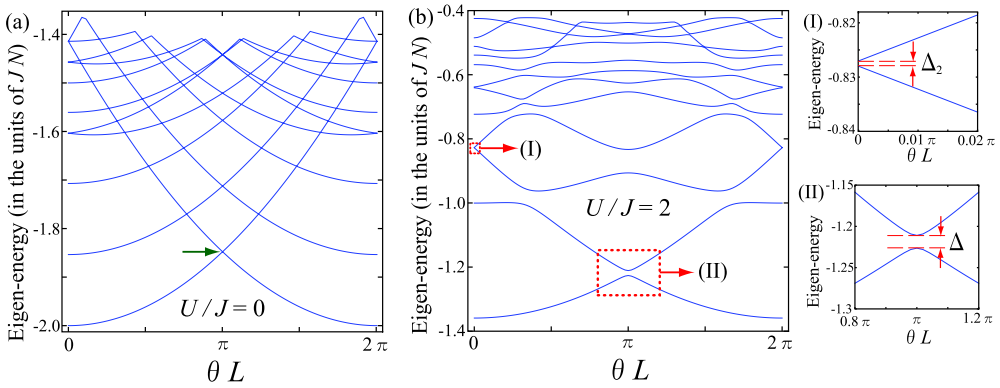

FIG. 15. (Color online) Twelve lowest energy levels with zero total quasimomentum of the Bose-Hubbard model with $L=8$ and $\nu=1$ as a function of θL. The two plots correspond to (a) $U=0$ and (b) $U=2J$. (I) and (II) are magnifications of the regions indicated in (b).

ence of a finite onsite interaction [see Fig. 15(b)], the degeneracy is broken and the emergence of the energy splitting is characterized as an avoided crossing of the two lowest-lying energy levels. Thus, the origin of the tunneling coupling between the two current states is the Umklapp-scattering process caused by the onsite interaction, which is a characteristic of a lattice system.

APPENDIX B: TEBD FOR LARGE FILLING FACTORS

In this appendix, we present an idea of adopting the TEBD method to the Bose-Hubbard model when the average number of particles per site ν (or the filling factor) is large. The key of the idea is that in addition to the upper bound, the lower bound for the occupation number of particle per site is introduced in order to significantly reduce the size of the local Hilbert space. This idea is crucial because the quantitative comparison of the TEBD results with the results of the instanton method based on the quantum rotor model is possible only for very large $\nu \gtrsim 1000$ (see Sec. IV).

Let us consider a system described by the 1D Bose-Hubbard model, Eq. (1) with L lattice sites. Spanning the Hilbert space of the whole system by a product of local Hilbert spaces of dimension d, a many-body wave function of the system is expressed as

$$|\Psi\rangle = \sum_{j_1,j_2,\ldots,j_L=1}^{d} c_{j_1,j_2,\ldots,j_L} |j_1\rangle |j_2\rangle \cdots |j_L\rangle. \tag{B1}$$

In the TEBD algorithm,[22] coefficients $c_{j_1,j_2,\ldots,j_L}$ are decomposed in a particular matrix product form as

$$c_{j_1,j_2,\ldots,j_L} = \sum_{\alpha_1,\ldots,\alpha_{L-1}=1}^{\chi} \Gamma^{[1]j_1}_{\alpha_1} \lambda^{[1]}_{\alpha_1} \Gamma^{[2]j_2}_{\alpha_1\alpha_2} \lambda^{[2]}_{\alpha_2} \cdots \lambda^{[L-2]}_{\alpha_{L-2}} \Gamma^{[L-1]j_{L-1}}_{\alpha_{L-2}\alpha_{L-1}} \times \lambda^{[L-1]}_{\alpha_{L-1}} \Gamma^{[L]j_L}_{\alpha_{L-1}}. \tag{B2}$$

The vector $\lambda^{[l]}_{\alpha_l}$ represents the coefficients of the Schmidt decomposition of $|\Psi\rangle$ with respect to the bipartite splitting of the system into $[1,\ldots,l-1,l]:[l+1,l+2,\ldots,L]$. The tensors Γ's constitute the Schmidt vectors together with the λ vectors. χ is the number of basis states, which is taken to be sufficiently large so that the error due to this truncation is nearly equal to zero. In our typical calculations, it ranges from $\chi=100$ to $\chi=250$.

Usually dimension of the local Hilbert space corresponding to a single site is chosen as $d=n_{\max}+1$, where $n_{\max}$ is the maximum number of particles per site. It is spanned by the basis set, $\{|n=0\rangle, |1\rangle, \ldots, |n_{\max}-1\rangle, |n_{\max}\rangle\}$. While, in principle, $n_{\max}$ is equal to the total number of particles in the system, taking much smaller $n_{\max}$ provides converged results in practice. For instance, for accurate determination of the zero-temperature phase diagram of the Bose-Hubbard model at unit filling, $n_{\max}=5$ ($d=6$) is sufficient.[41] At large filling factors, however, this choice of the local Hilbert space basis makes computations extremely expensive, because the computational cost in TEBD scales as $Ld^3\chi^3$. To solve this problem, in addition to $n_{\max}$, we introduce the minimum number of particles per site $n_{\min}$ and span the local Hilbert space by the basis set, $\{|n=n_{\min}\rangle, |n_{\min}+1\rangle, \ldots, |n_{\max}-1\rangle, |n_{\max}\rangle\}$, and thus $d=n_{\max}-n_{\min}+1$. In the parameter region of $U/(\nu J)\sim 1$, where our TEBD simulations are carried out, setting $n_{\max}=\nu+5$ and $n_{\min}=\nu-5$ corresponding to $d=11$ is sufficient for the convergence regardless of the value of ν. To

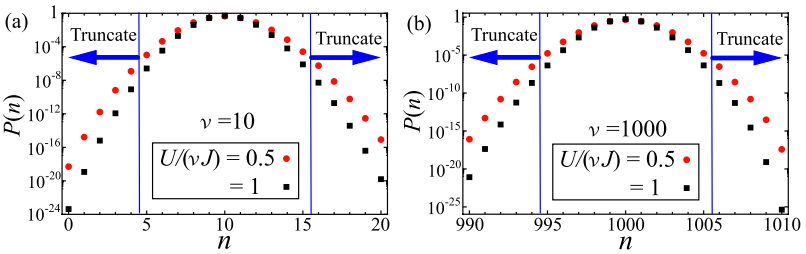

FIG. 16. (Color online) Occupation probabilities $P(n)$ (in the log-scale) of the local Fock state $|n\rangle$ in the ground state of the untwisted Bose-Hubbard model with (a) $\nu=10$ and (b) 1000, where $L=8$, and $U/(\nu J)=0.5$ (red circles) and 1.0 (black squares). Here L is the system size, ν is the filling factor, U is the onsite interaction and J is the hopping energy.

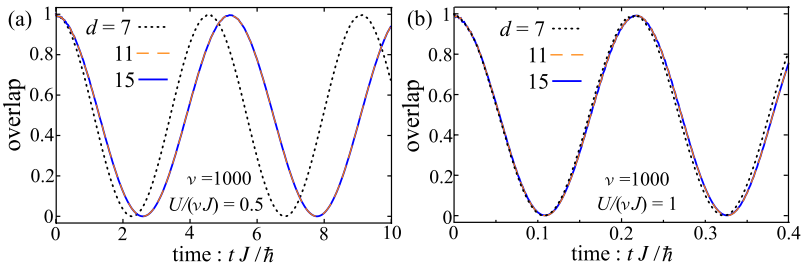

FIG. 17. (Color online) Time evolution of the overlap $|\langle\Phi_1|\Psi(t)\rangle|^2$ for several values of the local Hilbert space size d, where $L=8$, $\nu=1000$, and (a) $U/(\nu J)=0.5$ and (b) 1.

demonstrate this, in Fig. 16, we plot the occupation probabilities $P(n)$ of the local Fock state $|n\rangle$ in the ground state of the Bose-Hubbard model with the filling factor (a) $\nu=10$ and (b) $\nu=1000$. Here we set $L=8$, $\theta=0$, and $U/(\nu J)=0.5$ (red circles) and 1.0 (black squares). It is evident that $P(n)$ exponentially decays as n deviates from its average ν and that $P(n)$ for $n>\nu+5$ and $n<\nu-5$ is less than 10^{-6}. In addition, we present convergence tests for real-time dynamics with respect to d in Fig. 17, where the overlaps $|\langle\Phi_1|\Psi\rangle|^2$ for several values of d are plotted (see Sec. III for the definition of the overlap). Clearly, the results for $d=11$ are very well-converged. Thus, this truncation scheme of the local Hilbert space is justified both for the ground state and the real-time propagation. Note that when $U/(\nu J)<0.5$, we take $d=13$ ($n_{\max}=\nu+6$ and $n_{\min}=\nu-6$) for better convergence.

*Present address: RIKEN, Wako, Saitama 351-0198, Japan.

[1] M. Razavy, *Quantum Theory of Tunneling* (World Scientific, Singapore, 2003).
[2] S. Coleman, Phys. Rev. D **15**, 2929 (1977).
[3] C. G. Callan and S. Coleman, Phys. Rev. D **16**, 1762 (1977).
[4] A. M. Polyakov, Nucl. Phys. B **120**, 429 (1977).
[5] G. 't Hooft, Phys. Rev. Lett. **37**, 8 (1976).
[6] A. I. Vainstein, V. I. Zakharov, V. A. Novikov, and M. A. Shifman, Usp. Fiz. Nauk **136**, 553 (1982) [Sov. Phys. Usp. **25**, 195 (1982)].
[7] R. Rajaraman, *Solitons and Instantons* (North-Holland, Amsterdam, 1987).
[8] M. Ueda and A. J. Leggett, Phys. Rev. Lett. **80**, 1576 (1998).
[9] A. Polkovnikov, E. Altman, E. Demler, B. Halperin, and M. D. Lukin, Phys. Rev. A **71**, 063613 (2005).
[10] *Quantum Tunnelling in Condensed Media*, edited by Yu. Kagan and A. J. Leggett (North-Holland, Amsterdam, 1992).
[11] S. Takagi, *Macroscopic Quantum Tunneling* (Cambridge University Press, Cambridge, 2002).
[12] I. Chiorescu, T. Nakamura, C. J. P. M. Harmans, and J. E. Mooij, Science **299**, 1869 (2003).
[13] B. Sakita, *Quantum Theory of Many-Variable Systems and Fields* (World Scientific, Singapore, 1985).
[14] J. S. Langer, Phys. Rev. Lett. **21**, 973 (1968).
[15] M. H. Devoret, D. Esteve, C. Urbina, J. Martinis, A. Cleland, and J. Clarke, *Quantum Tunnelling in Condensed Media*, edited by Yu. Kagan and A. J. Leggett (Ref. 10).
[16] S.-X. Li, Y. Yu, Y. Zhang, W. Qiu, S. Han, and Z. Wang, Phys. Rev. Lett. **89**, 098301 (2002).
[17] C. D. Fertig, K. M. O'Hara, J. H. Huckans, S. L. Rolston, W. D. Phillips, and J. V. Porto, Phys. Rev. Lett. **94**, 120403 (2005).
[18] J. Mun, P. Medley, G. K. Campbell, L. G. Marcassa, D. E. Pritchard, and W. Ketterle, Phys. Rev. Lett. **99**, 150604 (2007).
[19] I. Danshita and C. W. Clark, Phys. Rev. Lett. **102**, 030407 (2009).
[20] C. Ryu, M. F. Andersen, P. Cladé, V. Natarajan, K. Helmerson, and W. D. Phillips, Phys. Rev. Lett. **99**, 260401 (2007).
[21] K. Henderson, C. Ryu, C. MacCormick, and M. G. Boshier, New J. Phys. **11**, 043030 (2009).
[22] G. Vidal, Phys. Rev. Lett. **93**, 040502 (2004).
[23] I. Danshita and P. Naidon, Phys. Rev. A **79**, 043601 (2009).
[24] S. Sachdev, *Quantum Phase Transitions* (Cambridge University Press, Cambridge, 1999).
[25] M. P. A. Fisher, P. B. Weichman, G. Grinstein, and D. S. Fisher, Phys. Rev. B **40**, 546 (1989).
[26] D. W. Hallwood, K. Burnett, and J. Dunningham, New J. Phys. **8**, 180 (2006).
[27] A. M. Rey, K. Burnett, I. I. Satija, and C. W. Clark, Phys. Rev. A **75**, 063616 (2007).
[28] S. R. White and A. E. Feiguin, Phys. Rev. Lett. **93**, 076401 (2004).
[29] U. Schollwöck, Rev. Mod. Phys. **77**, 259 (2005).
[30] G. Watanabe and C. J. Pethick, Phys. Rev. A **76**, 021605(R) (2007).
[31] A. Nunnenkamp, A. M. Rey, and K. Burnett, Phys. Rev. A **77**, 023622 (2008).
[32] L. Amico, A. Osterloh, and F. Cataliotti, Phys. Rev. Lett. **95**, 063201 (2005).
[33] B. L. Tolra, K. M. O'Hara, J. H. Huckans, W. D. Phillips, S. L. Rolston, and J. V. Porto, Phys. Rev. Lett. **92**, 190401 (2004).
[34] J. A. Freire, D. P. Arovas, and H. Levine, Phys. Rev. Lett. **79**, 5054 (1997).
[35] M. Nishida and S. Kurihara, J. Phys. Soc. Jpn. **68**, 3778 (1999).
[36] V. Ambegaokar, B. I. Halperin, D. R. Nelson, and E. D. Siggia, Phys. Rev. Lett. **40**, 783 (1978); Phys. Rev. B **21**, 1806 (1980).
[37] S. L. Sondhi, S. M. Girvin, J. P. Carini, and D. Shahar, Rev. Mod. Phys. **69**, 315 (1997).
[38] D. E. McCumber and B. I. Halperin, Phys. Rev. B **1**, 1054 (1970).
[39] L. S. Levitov and G. B. Lesovik, Pis'ma Zh. Eksp. Teor. Fiz. **58**, 225, (1993) [JETP Lett. **58**, 230 (1993)]; L. S. Levitov, H.-W. Lee, and G. B. Lesovik, J. Math. Phys. **37**, 4845 (1996).
[40] J. Schachenmayer, G. Pupillo, and A. J. Daley, New J. Phys. **12**, 025014 (2010).
[41] T. D. Kühner, S. R. White, and H. Monien, Phys. Rev. B **61**, 12474 (2000).